A biological vision inspired framework for machine perception of abutting grating illusory contours

Xiao Zhang[1], Kai-Fu Yang[1*], Xian-Shi Zhang[1], Hong-Zhi You[1]
Hong-Mei Yan[1], Yong-Jie Li[1*]
[1] Sichuan Cancer Hospital & Institute, School of Life Science and Technology,
University of Electronic Science and Technology of China.
xxyh0201@gmail.com; {yangkf, liyj}@uestc.edu.cn

Abstract

Higher levels of machine intelligence demand alignment with human perception and cognition. Deep neural networks (DNN) dominated machine intelligence have demonstrated exceptional performance across various real-world tasks. Nevertheless, recent evidence suggests that DNNs fail to perceive illusory contours like the abutting grating, a discrepancy that misaligns with human perception patterns. Departing from previous works, we propose a novel deep network called illusory contour perception network (ICPNet) inspired by the circuits of the visual cortex. In ICPNet, a multi-scale feature projection (MFP) module is designed to extract multi-scale representations. To boost the interaction between feedforward and feedback features, a feature interaction attention module (FIAM) is introduced. Moreover, drawing inspiration from the shape bias observed in human perception, an edge detection task conducted via the edge fusion module (EFM) injects shape constraints that guide the network to concentrate on the foreground. We assess our method on the existing AG-MNIST test set and the AG-Fashion-MNIST test sets constructed by this work. Comprehensive experimental results reveal that ICPNet is significantly more sensitive to abutting grating illusory contours than state-of-the-art models, with notable improvements in top-1 accuracy across various subsets. This work is expected to make a step towards human-level intelligence for DNN-based models.

1. Introduction

Contour perception is one of the most important components of visual perception of both human and machine, since contours convey essential information about object shapes and serve as a pivotal cue for figure-ground segregation [1]. Typically, contour perception arises at regions where pixel values change abruptly; however, even without stimulation from color contrast or luminance gradients, human visual system can still perceive clear boundaries [2]. Such boundaries are defined as illusory contours [3], also known as subjective or anomalous contours [4]. As a canonical visual illusion, illusory contours offer an invaluable window into understanding the neural mechanisms and computations underlying visual perception [5–10]. Research in cognitive psychology and neurophysiology indicates that the perception of illusory contours involves multiple mechanisms including cortical circuits [9, 11], visual attention [12], and perceptual organization [3, 13], constituting an intricate perceptual process. Beyond humans, this perceptual ability is also widely discovered in other biological visual systems, such as rodents [11], non-human primates [14], fish [15, 16], and birds [17]. In a way, the ability of perceiving illusory contours promotes the robustness of visual systems in processing incomplete and ambiguous visual inputs [5, 18, 19].

On the other hand, Deep Neural Networks (DNNs) have achieved and even surpassed human benchmarks in various computer vision tasks, such as image classification [20–22] and edge detection [23, 24]. To some extent, the development of DNNs has benefited from the advancements in neuroscience. A clear instance is the hierarchical architecture of DNNs, which is directly inspired by the visual neural mechanisms of cats [25, 26]. Nevertheless, Fan et al. [27] and Baker et al. [28] have pointed out that current convolutional neural network (CNN) and Transformer-based DNNs lack the ability to perceive illusory contours. For example, in certain cognitive psychology tasks, such as the classification of abutting grating illusion images [27], DNNs still perform poorly. These models fail to account for the experimental results from cognitive psychology [29]. Even the state-of-the-art large vision-language models (LVLMs) also show substantial discrepancies with humans in the perception of visual illusions [30].

Taken together, illusory contour perception is a funda-

*Corresponding author.

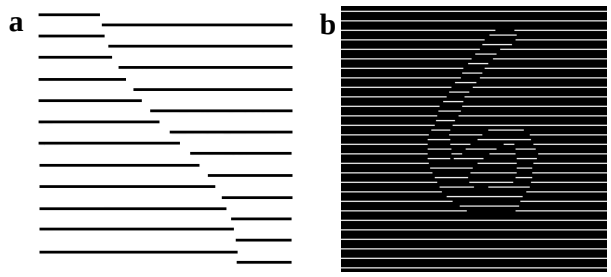

Figure 1. Demonstration of illusory contours. **a.** An abutting grating illusion with a simple curve, modified from Kanizsa [4]. **b.** An abutting grating illusion with a handwritten digit "6" from the AG-MNIST dataset [27].

mental capability in biological visual perception. To achieve human-like intelligence, DNNs should also possess such perceptual ability. However, the truth is that a significant misalignment persists between DNNs and humans in terms of perceiving illusory contours, which contradicts the ultimate goal of artificial intelligence (AI) [31]. Constructing DNNs models capable of perceiving illusory contours is expected to provide novel insights into utilizing physiological mechanisms to guide the design of neural networks with more human-like intelligence.

Here, we investigate how to construct a deep neural network with the capability of perceiving abutting grating illusory contours by drawing inspiration from the visual neural mechanisms. Specifically, inspired by inter- and intracortical circuits in the visual cortex, we propose a novel deep neural network with feedback connections, termed illusory contour perception network (ICPNet), which demonstrates enhanced perception along the abutting grating illusory contours (see Fig. 1 for examples). To the best of our knowledge, ICPNet is the first neural network with a significant ability to perceive the abutting grating illusory contours. Furthermore, rather than relying on a single convolutional layer in the initial layers of networks, a special block is designed to extract multi-scale representations of the input. To effectively integrate features from feedforward and feedback pathways, we then develop a feature interaction attention module (FIAM). Moreover, building upon the shape bias in human visual perception [32], we combine the edge detection task and the image classification task by introducing shape constraints into our network. An intriguing consequence of this multi-task learning framework is that ICPNet exhibits increased focus on global contours and foreground information, aligning with the principles of visual perception [32–34]. Ultimately, to enhance the diversity of abutting grating illusory images, we contribute the AG-Fashion-MNIST test set. Comprehensive experimental results on the AG-MNIST and AG-Fashion-MNIST test sets demonstrate that our proposed ICPNet possesses superior illusory contour perception performance compared to other state-of-the-art computational models.

2. Related Work

Neural mechanisms of illusory contour perception. The neural mechanisms of illusory contour perception have attracted widespread interest in neuroscience. Initially, some scholars argued that such perception relied solely on interaction in early visual cortices, namely the primary visual cortex (V1) and the secondary visual cortex (V2) [35–40]. However, in illusory contour figures such as the Kanizsa triangle [41], when the distance between the inducers exceeds a certain threshold, the neurons in V1/V2 no longer respond to the illusory contours [39]. In contrast, human vision generally encompasses long-range illusory contour perception [42]. Meanwhile, the perception of illusory contours is critically and permanently impaired by higher-order visual cortex lesions [43, 44]. Therefore, it was proposed that illusory contour perception also depends on neurons with larger receptive fields (RF), indicating that higher-order cortical areas mediate the formation of illusory contours [45]. Given these reflections, some researchers have elucidated that illusory contour perception is primarily shaped through feedback modulation from higher-order visual cortices, including V4, lateral occipital complex (LOC), and inferior temporal (IT) cortex [9, 11, 46–50]. In contrast to the above-mentioned studies, Cheng and colleagues leveraged DNNs to reconstruct the internal representations underlying illusory perception from functional magnetic resonance imaging (fMRI) data. Their findings indicate that abutting grating illusory contour perception involves a distributed network spanning V1 to V4 and higher-order cortical regions, such as LOC, with the perception mainly localized in early visual cortices [51].

In summary, physiological evidence highlights that illusory contour perception is a constructive process reliant on the interaction between lower- and higher-order visual cortical areas. Feedback modulation plays a crucial role in this perception besides feedforward connections.

Illusory contour perception of DNNs

Illusory contour perception fulfills its crucial role in enabling biological visual systems to interpret complex scene information [3, 52]. Baker and colleagues [28] explored whether DNN models used the same features as humans to perceive real and illusory contours, and concluded that DNNs lacked genuine illusory contour perception. Given that feedforward-based DNNs lacked feedback modulation, Lotter et al. [53] observed that the predictive coding [54] based on PredNet [55] model exhibited dynamic characteristics similar to those of superficial neurons in macaque V1/V2 while processing the Kanizsa square [4]. Therefore, they suggested that the predictive coding architecture reveals ac-

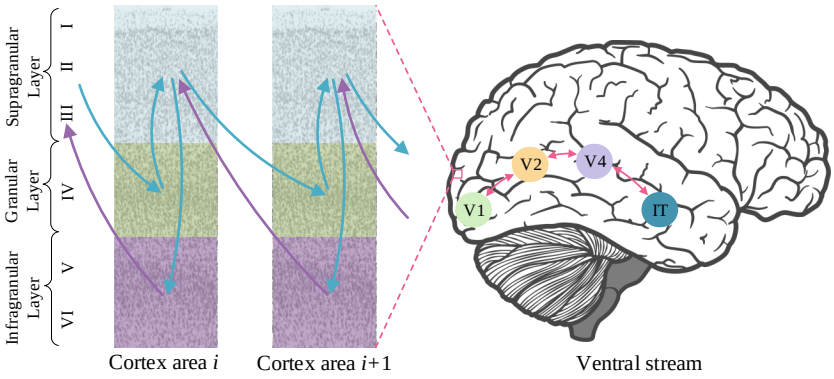

Figure 2. Schematic diagram of ventral stream, cortical structures, and circuits. Blue arrows denote feedforward circuits, while purple arrows represent feedback circuits.

tivation along the illusory contours. Furthermore, Pang et al. [56] combined predictive coding with CNN to construct a model capable of perceiving the Kanizsa square. They posited that the illusory contour perception of DNNs arose from self-supervised reconstruction training and feedback connections. Nevertheless, a major drawback of their model is that the classification result is obtained by averaging the outputs of nine sub-models.

In the aforementioned studies, the training and test images were typically generated by hand-crafted illusory contours popularly presented in psychological literature, such as Kanizsa square [4]. These manually designed datasets are limited in quantity, which hinders comprehensive evaluation of illusory contour perception of DNNs. Recently, Fan et al. [27] proposed a novel method for converting the MNIST dataset [57] into an abutting grating illusory contours dataset, thereby constructing the AG-MNIST test set. Models can be trained on the original MNIST training set and then their illusory contour perception capability can be directly evaluated on the AG-MNIST test set. They found that the performance of the vast majority of DNNs was close to random guessing by evaluating 109 models based on CNN and Transformer architectures, which supports the results of Cheng [51]. Differing from all previous works, Zhang et al. [30] assessed four LVLMs from the perspective of human-like visual illusion perception. They also observed that these models generally aligned poorly with human visual illusion perception.

Together, existing approaches for modeling illusory contour perception are difficult to transfer to real-world tasks and most current neural networks essentially lack the capability of perceiving illusory contours like the abutting grating. This work aims to construct DNNs with the power to detect illusory contours and distinguish figure from background by learning visual mechanisms, which is expected to help make a step towards human-level intelligence for DNN-based models.

3. Methodology

3.1. Preliminary

Cortical structures and circuits. Physiological studies have demonstrated that neurons in the primate cortex are organized into a columnar structure comprising six distinct layers (I∼VI) [58, 59], as shown in Fig. 2. Layers I∼III, layer IV, and layers V∼VI are respectively termed the supragranular layer (SL), granular layer (GL), and infragranular layer (IL). The cortex supports high-order cognitive functions [60] and is one of the most intricate structures in the brain. The GL primarily receives inputs from the SL of the previous cortical area and projects information to the SL of the current area [61]. Subsequently, the SL transmits information to the pyramidal neurons in the deeper IL [60] and receives feedback inputs from higher cortical areas [50].

Moreover, within the ventral stream (i.e., V1→V2→V4→IT) [62], as the cortical hierarchy progresses, the SL becomes significantly thicker and contains larger pyramidal neurons, accompanied by a thinning of the GL [63]. Such change supports the pivotal role of the SL in cortical information integration [60]. Although the IL is thinner than the SL, it likewise exhibits this trend [60, 63, 64]. Overall, this fundamental cortical organization provides the structural basis of our model for illusory contour perception.

3.2. ICPNet architecture

The overall architecture of ICPNet is illustrated in Fig. 3. This model adopts a multi-task learning framework, which includes classification task and edge detection task. For classification, the input image is first processed by the multi-scale feature projection (MFP) block to obtain multi-scale features. This is followed by four stages inspired by cortical structures and circuits, corresponding to V1, V2, V4, and IT areas, respectively. Each stage consists of three components, including the granular layer (GL), supragranular layer (SL),

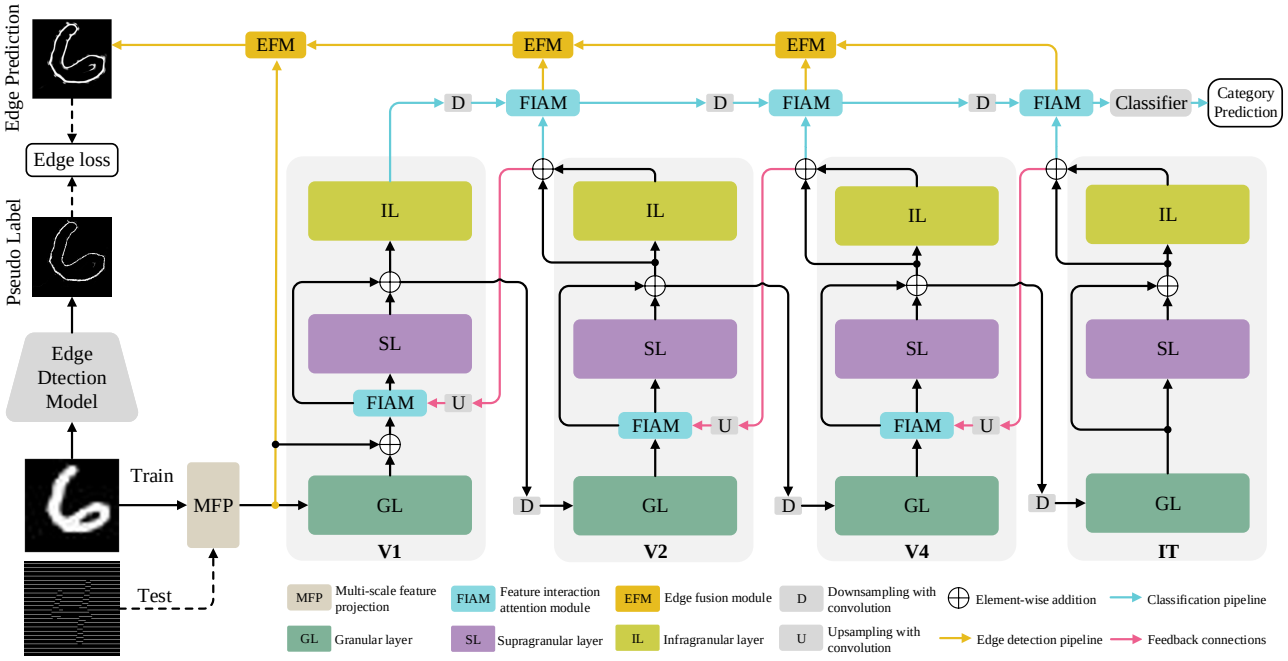

Figure 3. The overall architecture of ICPNet. Our network consists of two main pipelines: classification and edge detection. The former obtains outputs through four stages with feedback connections, while the latter employs a top-down structure to integrate side outputs via EFM to generate edge predictions. During the training phase, we freeze the network weights of the edge detection model pre-trained on the BSDS-VOC dataset [65, 66].

Table 1. Detailed parameters of four stages with a structure of [kernel size, channel number, dilation rate]. "r", "DW", and "Conv" indicate dilation rate, depthwise separable convolution, and vanilla convolution layer, respectively. "GL", "SL", and "IL" correspond to the granular layer, supragranular layer, and infragranular layer, respectively.

Block name	Stage 1	Stage 2	Stage 3	Stage 4
SL	[4×4DW, 128, r=2] [1×1Conv, 64, r=1]	[7×7DW, 128, r=2] [3×3DW, 256, r=6] [1×1Conv, 128, r=1]	[9×9DW, 256, r=3] [3×3DW, 512, r=12] [1×1Conv, 256, r=1]	[9×9DW, 512, r=3] [3×3DW, 1024, r=12] [1×1Conv, 512, r=1]
GL	[5×5DW, 64, r=1] [3×3DW, 128, r=2] [1×1Conv, 64, r=1]	[6×6DW, 128, r=2]	[7×7DW, 256, r=3]	[7×7DW, 512, r=3]
IL	[4×4DW, 64, r=2]	[7×7DW, 256, r=2] [1×1Conv, 128, r=1]	[9×9DW, 512, r=3] [1×1Conv, 256, r=1]	[9×9DW, 1024, r=3] [1×1Conv, 512, r=1]

and infragranular layer (IL). Regarding cortical connectivity, there is a massive network of functional connections both between and within cortical regions. To simplify neural network design, we only consider feedforward and feedback connections between adjacent cortices. Therefore, in addition to feedforward connections, feedback connections with global features are also established to simulate the modulation from V2 to V1 [67], V4 to V2 [68], and IT to V4 [69]. The feature interaction attention module (FIAM) is designed to integrate the feedback and feedforward features. Moreover, inspired by the shape bias in the visual system [32], we introduce the edge detection task to inject shape constraints into the network. The edge fusion module (EFM) merges side outputs with different resolutions in a top-down fashion to obtain the edge prediction. By jointly optimizing the both tasks, the network can concentrate more effectively on foreground information.

With the four stages, the convolutional kernels in each stage are designed according to the RF size of different cortical areas. Table 1 lists the detailed parameters of the four stages. Concretely, the average RF size of V2 is approximately twice that of V1 [70], and the average RF size of V4

is about twice that of V2 [71]. Therefore, in conjunction with the structural rationality of the network, the kernel sizes between stages maintain an approximate double relationship, except for the last two stages. Meanwhile, to control the number of parameters, dilated convolution [72] and depth-wise separable convolution (DW) [73] are utilized in the design of the basic convolutional blocks. Following ResNet architecture [21], the number of channel of four stages are set to 64, 128, 256, and 512, respectively. To align the size and channel number of feature maps, we employ downsampling and upsampling with convolution used in Swin [74]. Specifically, the upsampling with convolution is formulated as

$$f_u = Conv\left(LN\left(Up\left(\cdot\right)\right)\right), \tag{1}$$

where f_u is the aligned features. LN, $Conv$, and Up denote the layer normalization [75], a 1×1 convolution layer with stride 1, and the transposed convolution, respectively. Replacing bilinear upsampling with pooling results in the downsampling with convolution. Neurophysiological findings reveal that, besides the IT area, subcortical regions also interact with the IL of cortices to facilitate efficient object recognition [76–78]. Accordingly, we fuse side outputs from the IL via the FIAM in a bottom-up fashion. The final output is then fed into the classifier to implement classification. The classifier is defined as

$$P_{cls} = softmax\left(FC\left(LN\left(GAP\left(\cdot\right)\right)\right)\right), \tag{2}$$

where P_{cls} is the classification probability. FC and GAP are a fully-connected layer and a global average pooling layer, respectively.

3.3. Multi-scale feature projection (MFP)

In general, the initial layers of the model focus on how to process images at the beginning of a neural network and typically apply a single-layer convolution to extract initial features. For instance, CovNeXt [79] employs a 4×4 non-overlapping convolutional layer with stride 4 as the stem. However, multi-scale features are critical for CNN perception [80]. Therefore, we develop MFP with dilated convolution to extract multi-scale representations, as shown in Fig. 4a. In the MFP block, the input image first passes through convolutional layers with stride 2 and different dilation rates in parallel, and the resulting feature maps are summed together, followed by LN. To further enhance the interaction among the representations, we apply a channel shuffle [81] to obtain the final output. Although the MFP module is relatively simple, our ablation studies demonstrate that the multi-scale features is essential for abutting grating illusory contour perception.

3.4. Feature interaction attention module (FIAM)

As shown in Fig. 4b, to better integrate features from different levels, we construct the FIAM built upon the CBAM [82]. For feedback connections, the features from the higher-level stages (i.e., input_2) first undergo upsampling with convolution to align the size and channel number with that of the lower-level stages. These features are then added to the low-level features (i.e., input_1) that have been processed by channel attention. Here, spatial average pooling and spatial max pooling refer to pooling performed on each channel individually, sharing the same convolutional layers. The number of output channels of the channel attention module is consistent with that of the features from the lower-level stage. Following ConvNeXt [79], the expansion factor k is set to 4. Subsequently, the output of the channel attention module is fed into multi-scale spatial attention. Inspired by CSWin [83], we design multi-scale cross-shaped convolutional kernels within the spatial attention to capture a broader range of contextual information with as few parameters as possible. The channel average pooling and channel max pooling refer to pooling along the channel axis. For the side outputs, features from the lower-level stages are first aligned in size and channel number via downsampling with convolution, and then the attention operation is conducted on the inputs. The channel number of the final output is set to match that of the features from the higher-level stage.

3.5. Edge fusion module (EFM)

The human visual system exhibits shape bias in object recognition [32]. Accordingly, the edge detection task is introduced to provide shape constraints. To achieve edge prediction, we design a simple decoder composed of the EFM. Moreover, we utilize the decoder of the frozen LVP-Net [84] pre-trained on the BSDS-VOC dataset [65, 66] to generate pseudo labels for edge prediction. As illustrated in Fig. 4c, inputs with different resolutions are individually processed through a convolutional layer, LN, and GELU activation [85]. The lower-resolution input is then upsampled using bilinear interpolation and added to the other inputs. After several EFMs, an edge prediction map is generated via bilinear upsampling, a 3×3 convolutional layer, and a sigmoid function in sequence.

3.6. Network training

To simultaneously optimize the edge detection task and the classification task, we define a multi-task learning loss function L_{total} as follows:

$$L_{total} = L_{cls} + \gamma \cdot L_{edge}, \tag{3}$$

where L_{cls} and L_{edge} represent the classification loss and the edge loss, respectively. γ is the fusion weight. In the ablation study, we carefully assess the impact of γ on network performance in Table 5.

The classification loss L_{cls} is defined as multi-class cross-

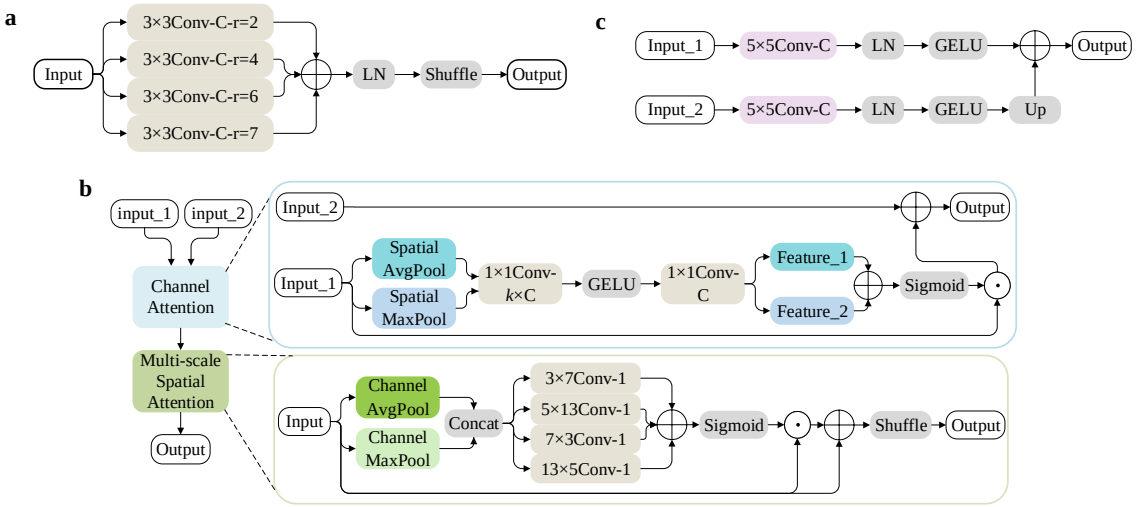

Figure 4. The detailed structures of submodules. **a.** MFP. "C" is equal to 64. "r" and "$\oplus$" denote dilation rate and element-wise addition, respectively. **b.** FIAM. FIAM is composed of the channel attention and the multi-scale spatial attention. "input_1" and "input_2" indicate the features from the lower-level stage and the higher-level stage, respectively. "$\odot$", "k", and "C" denote element-wise multiplication, expansion factor, and channel number, respectively. **c.** EFM. "Up" denotes the bilinear upsampling.

entropy, which is formulated as

$$L_{cls}\left(P_{cls}, Y_{cls}\right) = -\frac{1}{N}\sum_{i=0}^{N-1}\sum_{j=0}^{M-1} Y_{cls}^{ij}\log\left(P_{cls}^{ij}\right), \quad (4)$$

where Y_{cls} and P_{cls} is the class labels and predictions, respectively. The shape of P_{cls} and Y_{cls} is $N\times M$, where N and M represents the sample size of a batch and the total classes, respectively. Y_{cls}^{ij} is the $(i,j)^{th}$ label of Y_{cls}, while P_{cls}^{ij} is the $(i,j)^{th}$ probability of P_{cls}.

Due to the highly imbalanced distribution of positive and negative samples in the edge maps, we employ the class-balanced cross-entropy loss function proposed in HED [86] as our edge loss. Following HED and LVP-Net [84], for an edge pseudo label $Y_{edge} = \{y_j, j = 1, ..., |Y_{edge}|\}$, $y_j \in [0, 1]$, we fist define the edge positive sample set and the edge negative sample set as $Y^+ = \{y_j, y_j > \eta\}$ and $Y^- = \{y_j, y_j = 0\}$, respectively. η is a threshold used to exclude ambiguous edge pixels. The other pixels are neglected. Given an edge prediction map $P_{edge} = \{p_j, j = 1, ..., |P_{edge}|\}$, $p_j \in [0, 1]$, the edge loss function is formulated as

$$L_{edge}\left(P_{edge}, Y_{edge}\right) = -\alpha\sum_{j\in Y^-}\log\left(1-p_j\right) - \beta\sum_{j\in Y^+}\log\left(p_j\right), \quad (5)$$

where

$$\alpha = \lambda\cdot\frac{|Y^+|}{|Y^+|+|Y^-|}, \quad (6)$$

$$\beta = \frac{|Y^-|}{|Y^+|+|Y^-|}. \quad (7)$$

Here, p_j is an edge probability value computed using the sigmoid function at the j^{th} pixel. α and β are the weights to control the balance between positive and negative samples. λ is an empirical coefficient to adjust the weights of edge and non-edge loss.

4. Experiments

4.1. Datasets

We evaluated the capability of perceiving abutting grating illusory contours of various DNN models on the AG-MNIST [27] and AG-Fashion-MNIST test sets. MNIST [57] is a well-known handwritten digit image dataset that contains 60,000 training images and 10,000 testing images across ten categories. The AG-MNIST test set was constructed based on the abutting grating illusion and the MNIST test set. In this paper, the AG-MNIST test set comprises various types of images, which are generated by the abutting gratings in four orientations with six different pixel intervals between grating lines. AG-MNIST shares the same categories as MNIST. Following Fan et al. [27], since the small size of the original MNIST images, the AG-MNIST test set upsamples the original images to 224×224 to retain more details. Fig. 5 shows some examples.

To further evaluate the perception of abutting grating illusory contours, we transformed the more challenging Fashion-MNIST test set [87] into the abutting grating illusory images. The Fashion-MNIST dataset comprises ten categories totaling 70,000 grayscale images of fashion products, with 7,000 images per category. The training set and test set consist of 60,000 and 10,000 images, respectively. We first

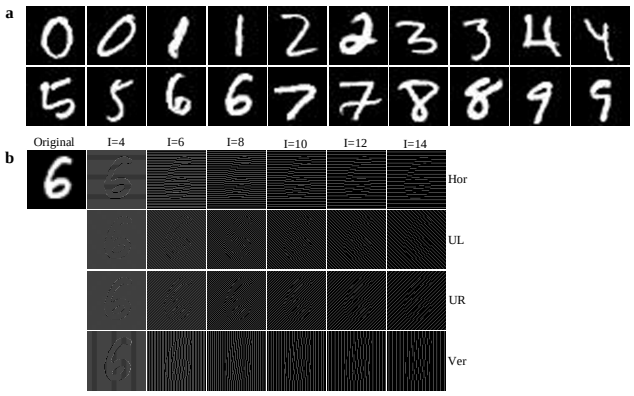

Figure 5. Examples in the MNIST and AG-MNIST test sets. **a.** Demonstration of some original handwritten digit images in the MNIST test set totaling ten categories, with two images per category. **b.** Demonstration of the abutting grating illusion images in the AG-MNIST test set, generated with four orientation gratings. "I" denotes the pixel interval between grating lines. "Hor", "UL", "UR", and "Ver" represent the illusory contour generated via horizontal, diagonal from upper left to lower right, diagonal from upper right to lower left, and vertical abutting gratings, respectively.

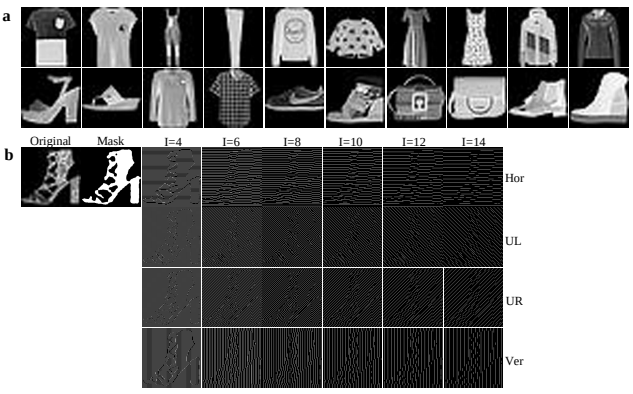

Figure 6. Examples in the Fashion-MNIST and AG-Fashion-MNIST test sets. **a.** Demonstration of some original fashion product images in the Fashion-MNIST test set totaling ten categories, with two images per category. **b.** Demonstration of the abutting grating illusion images in the AG-Fashion-MNIST test set, generated with four orientation gratings. "I" denotes the pixel interval between grating lines. "Hor", "UL", "UR", and "Ver" represent the illusory contour generated via horizontal, diagonal from upper left to lower right, diagonal from upper right to lower left, and vertical abutting gratings, respectively.

extracted the masks from the Fashion-MNIST test set via the Segment Anything Model (SAM) [88] and manually removed the inaccurate masks. For mutual complementarity, the Fashion-MNIST test set was also binarized by the OTSU method [89] and the poorly binarized images were manually deleted. Subsequently, the two groups of images were mixed together to preserve as much of the test images as possible. Finally, the abutting grating distortion method [27] was applied to the binarized images to generate the illusory images. The resulting test set is named the AG-Fashion-MNIST test set, which contains 8,916 abutting grating images. Fig. 6 exhibits some examples.

With the AG-MNIST and AG-Fashion-MNIST test sets, we can directly and quantitatively assess the abutting grating illusory contour perception ability of networks without the need for model fine-tuning or modifications to the classifier. Moreover, the AG-Fashion-MNIST test set is particularly suitable for researchers with limited computational resources due to its small scale.

4.2. Implementation details

In this study, we trained eight models from scratch on the MNIST and Fashion-MNIST training set, including VGG16 [90], ResNet18 [21], ResNet101 [21], ViT-L-16 [20], Swin-B [74], ConvNeXt-B [79], MambaOut-B [91], and our proposed ICPNet. All models were evaluated on both the original and AG test sets. Our network was initialized from zero-mean Gaussian distribution with a standard deviation of 0.02. For the edge detection task, following previous work [84, 86], the threshold η and the coefficient λ were set to 0.2 and 1, respectively.

For fairness, we maintained consistent hyperparameters as much as possible. To stabilize the training for ConvNeXt-B and MambaOut-B, we employed the AdamW [92] optimizer with the initial learning rates of 1×10^{-3} and 4×10^{-4}, respectively. Our ICPNet was trained using SGD with an initial learning rate of 1×10^{-3} to facilitate the convergence of both loss functions. The remaining models were optimized using SGD with an initial learning rate of 1×10^{-2}. The momentum and batch size were set to 0.9 and 40, respectively. We adopted a standard input resolution of 224×224. Following Fan et al. [27], all models were trained for 100 epochs, with the best-performing model on the original test sets selected for subsequent evaluation. Aside from random horizontal flipping, no additional tricks were applied, aiming to focus solely on the network architecture. All experiments were conducted on an NVIDIA 3090 GPU with 24GB of memory.

4.3. Ablation study

We conducted systematic ablation experiments to evaluate the model from multiple perspectives. Our network was trained on the MNIST training set and evaluated on both the MNIST and AG-MNIST test sets. As shown in Table 2, for clarity, we first divided the experiments into six groups, including receptive field (RF) size, feedback interaction, MFP, FIAM, and EFM. The detailed quantitative results are provided in Table 3.

Overall, each component contributes to the improvement

Table 2. Ablation experiment groups.

Experiments	RF size	Feedback	MFP	FIAM	EFM
Group 1	×	×	×	×	×
Group 2	√	×	×	×	×
Group 3	√	√	×	×	×
Group 4	√	√	√	×	×
Group 5	√	√	√	√	×
Group 6	√	√	√	√	√

Table 3. Ablation experiments of RF size, feedback, MFP, FIAM, and EFM. The first row of results is obtained on the original MNIST test set. Bold denotes the best top-1 accuracy.

Dataset		Group 1 (Top-1 Acc.(%))	Group 2 (Top-1 Acc.(%))	Group 3 (Top-1 Acc.(%))	Group 4 (Top-1 Acc.(%))	Group 5 (Top-1 Acc.(%))	Group 6 (Top-1 Acc.(%))
MNIST (Original)		99.58	99.45	99.55	99.49	99.62	99.49
I=4	Hor	28.37	34.35	49.02	27.80	31.36	**81.27**
	UL	17.97	19.18	19.09	11.59	18.75	**77.72**
	UR	24.52	19.36	16.65	18.25	26.87	**70.94**
	Ver	19.17	23.16	22.56	11.20	25.17	**67.43**
I=6	Hor	18.06	57.09	49.70	97.02	**98.54**	98.15
	UL	13.78	19.52	40.89	97.93	**98.85**	98.73
	UR	14.78	18.45	34.76	98.25	**98.91**	98.81
	Ver	19.44	47.48	48.43	98.01	**98.61**	98.50
I=8	Hor	29.88	26.96	20.46	26.50	37.69	**42.46**
	UL	13.13	16.66	24.98	23.37	32.02	**58.22**
	UR	20.54	14.28	23.32	24.25	38.53	**49.48**
	Ver	**62.51**	23.19	42.13	20.39	41.59	35.22
I=10	Hor	15.42	21.48	17.93	82.65	**94.97**	94.33
	UL	19.34	15.01	38.11	93.25	**98.46**	97.55
	UR	14.75	13.71	25.58	94.53	**98.47**	98.08
	Ver	16.74	17.06	16.47	83.97	94.10	**95.90**
I=12	Hor	13.10	16.81	12.44	14.83	10.45	**38.28**
	UL	11.67	15.02	22.82	10.98	24.51	**35.26**
	UR	19.23	12.38	18.56	9.91	21.84	**37.73**
	Ver	11.84	12.69	9.88	11.29	16.41	**27.89**
I=14	Hor	11.27	12.60	22.47	83.30	**94.83**	77.45
	UL	14.44	13.82	41.10	92.50	**98.49**	93.15
	UR	14.99	11.88	31.63	89.81	**98.13**	96.18
	Ver	13.59	15.58	10.85	68.18	**95.32**	86.09

of the abutting grating illusory contours perception. In Group 1, all convolutional kernels across stages are uniformly set to 3×3, whereas Group 2 employs kernel configurations according to Table 1. As shown in Table 3, despite adopting a purely feedforward mode, the top-1 accuracy of Group 1 overall surpasses that of most of the methods reported in Table 6. Compared with Group 1, Group 2 exhibits significant accuracy improvements at grating line intervals of 4 and 6. These results confirm the effectiveness of the foundational configurations. Upon incorporating feedback connections, the network exhibits further improvements, especially at the larger intervals of 10, 12, and 14. This finding indicates that feedback modulation with global information contributes to illusory contour perception, which is consistent with the discoveries of Pak et al. [11] and Pan et al. [9]. In Group 4, multi-scale RF significantly enhances accuracy at the intervals of 6, 10, and 14. Moreover, FIAM facilitates a comprehensive fusion of representations, boosting perfor-

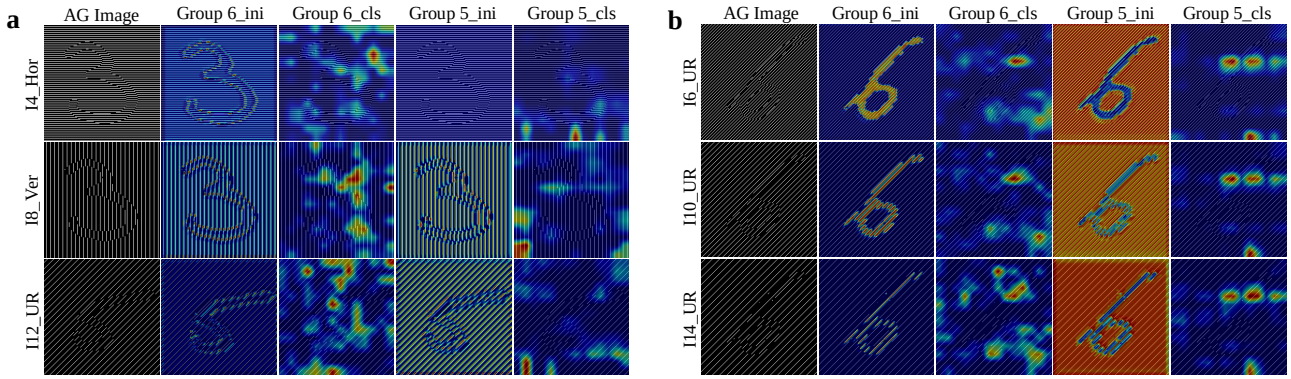

Figure 7. Visual explanations of the abutting grating illusion images. **a.** Visual explanations of the illusion images with intervals of 4, 8, and 12 generated by Grad-CAM. **b.** Visual explanations of the illusion images with intervals of 6, 10, and 14 generated by Grad-CAM. "ini" indicates the visualizations of the input features of the first stage, while "cls" represents the visualizations of the output features from the final convolutional layer of the network.

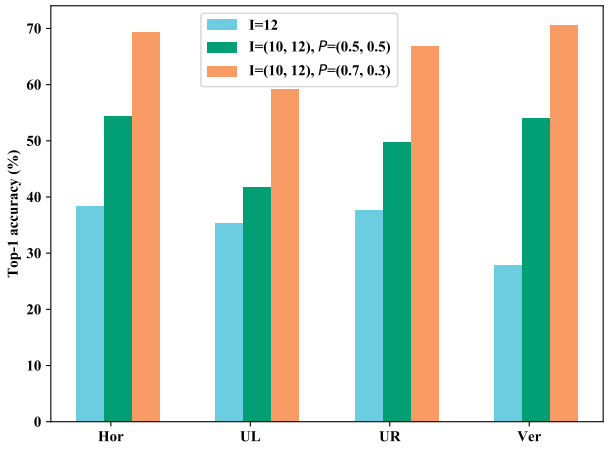

Figure 8. The top-1 accuracy on the abutting grating illusion images with randomly varying intervals. "I=(10, 12), P=(0.7, 0.3)" denotes the abutting gratings with intervals of 10 and 12 appear in each image with probabilities of 0.7 and 0.3, respectively.

mance across most pixel intervals. Finally, edge detection based on the EFM provides shape constraints for the model. Although the results for the intervals of 6, 10, and 14 slightly decreased, the constraint markedly improves the top-1 accuracy at the intervals of 4, 8, and 12. Collectively, these results validate the complementary functionality of each module.

For analyzing shape constraints, we employed Grad-CAM [93] to visualize features for Group 5 and Group 6, as shown in Fig. 7. These examples were all correctly classified by the networks. First, it can be observed that the network indeed pays more attention to the foreground and the illusory contours after incorporating shape constraints, which aligns more closely with human intuition. Conversely, although the results of classification are correct, the visualizations

Table 4. The effect of the number of grating lines on top-1 accuracy. The first row corresponds to the deleted proportions of grating lines.

Dataset		0%	10%	20%	40%	80%
I=6	Hor	98.15	95.74	91.62	71.18	22.69
	UL	98.73	97.91	96.29	87.82	36.62
	UR	98.81	98.24	96.95	90.66	36.40
	Ver	98.50	96.74	94.62	82.86	34.05

for Group 5 tend to emphasize background informatiosn. Specifically, the visualizations of Group 6 for intervals of 6, 10, and 14 to some extent validate the complementarity between oriented illusory contour perception and non-oriented surface brightness filling-in [34].

In conjunction with both quantitative and qualitative results, we posit that the reduced accuracy of ICPNet at certain intervals may stem from an intrinsic perceptual bias within the network, which impairs its ability to perceive abutting grating illusory contours at these intervals. In fact, the interval-dependent bias has been also reported in human experiments [94]. To verify this hypothesis, we evaluated the performance of ICPNet on abutting grating images with randomly varying intervals. As shown in Fig. 8, compared to the grating images only with interval 12, increasing the proportion of interval 10 leads to the pronounced gains in top-1 accuracy, which proves our hypothesis.

Moreover, to examine the effect of the number of grating lines on top-1 accuracy, we conducted experiments at the grating images of interval 6, where we randomly deleted varying proportions of grating lines, as shown in Table 4. The results reveal that the accuracy of ICPNet consistently declines as grating lines are removed, with a steep drop observed at the proportions of 40% and 80%. These results align with previous observations that sparser grating

Table 5. The impact of the fusion weight γ on ICPNet. The first row of results is obtained on the original MNIST test set. Bold denotes the best top-1 accuracy.

Dataset		γ=0.004	γ=0.008	γ=0.01	γ=0.02	γ=0.04
		Top-1 Acc.(%)	Top-1 Acc.(%)	Top-1 Acc.(%)	Top-1 Acc.(%)	Top-1 Acc.(%)
MNIST(Original)		99.49	99.45	99.49	99.55	99.28
I=4	Hor	29.08	37.93	**81.27**	60.34	15.32
	UL	63.81	44.93	**77.72**	44.13	12.67
	UR	53.85	41.60	**70.94**	55.79	18.44
	Ver	35.57	35.98	**67.43**	30.27	13.32
I=6	Hor	97.99	**98.29**	98.15	97.37	97.29
	UL	98.44	98.49	**98.73**	97.23	94.16
	UR	**98.85**	98.35	98.81	97.74	91.79
	Ver	97.82	98.35	**98.50**	97.74	92.06
I=8	Hor	34.29	37.37	**42.46**	36.94	29.38
	UL	41.42	**59.47**	58.22	36.43	28.10
	UR	26.81	32.54	**49.48**	29.56	28.02
	Ver	25.87	**36.17**	35.22	28.49	23.61
I=10	Hor	88.34	89.03	**94.33**	91.26	66.67
	UL	97.35	97.10	**97.55**	96.65	89.82
	UR	**98.15**	97.04	98.08	98.09	83.51
	Ver	86.96	94.01	**95.90**	94.17	84.17
I=12	Hor	27.36	23.27	**38.28**	25.29	25.34
	UL	**38.51**	25.67	35.26	33.56	20.32
	UR	26.21	20.32	**37.73**	22.65	10.84
	Ver	19.29	12.97	**27.89**	18.49	11.07
I=14	Hor	75.92	69.90	**77.45**	71.22	54.41
	UL	**96.15**	93.25	93.15	95.71	85.28
	UR	**96.31**	95.99	96.18	94.80	73.84
	Ver	81.65	82.95	**86.09**	80.07	55.72

lines typically accompany weaker illusory contour perception strength [38, 94].

Finally, we evaluated the impact of the fusion weight γ of the multi-task loss function on ICPNet. As shown in Table 5, the suboptimal fusion leads to a significant degradation in the top-1 accuracy of abutting grating illusory images. In this study, the fusion weight γ is set to 0.01.

4.4. Comparison with state-of-the-art methods

Performance comparison on AG-MNIST. We compare ICPNet with several representative DNN models, including VGG16 [90], ResNet18 [21], ResNet101 [21], ViT-L-16 [20], Swin-B [74], ConvNeXt-B [79], and MambaOut-B [91]. All methods were trained from scratch on the MNIST training set [57] and then directly evaluated on the AG-MNIST test set [27]. The ICPNet variant with only feedback connections (i.e., Group 3 in Table 3) is selected as the baseline. The detailed quantitative results are presented in Table 6.

The quantitative results indicate that our approach exhibits a significant ability to perceive abutting grating illusory contours and our top-1 accuracy substantially outperforms that of state-of-the-art methods across most pixel intervals. Specifically, ICPNet achieves the average top-1 accuracy of 89.39% at intervals of 4, 6, 10, and 14. Although the accuracy at intervals of 8 and 12 is relatively lower, it is still superior to most methods. We think the relative degradation of our model at these two intervals may stem from an intrinsic perceptual bias, as illustrated in Fig. 8. Notably, the top-1 accuracy of the baseline exceeds that of other methods on most subsets, underscoring the effectiveness of our feedback-based architecture. On the other hand, Swin attains a top-1 accuracy of 95.74% for the UL gratings of interval 4, which may suggest an advantage of Transformers in long-range perception. However, on the other subsets, Swin performed near the random level. Overall, these results highlight the superiority of ICPNet and indicate that existing methods generally lack the capability of perceiving abutting grating illusory contours, which is consistent with the findings of Fan et al. [27].

We also utilized Grad-CAM [93] to generate visual explanations, as shown in Fig. 9. The edge maps indicate that our approach predicts the abutting grating illusory contours

Table 6. Quantitative comparison on MNIST and AG-MNIST test sets. The human data derives from the work of Fan et al. [27]. The first row of results is obtained on the original MNIST test set. Group 3 in Table 3 is selected as the baseline. The best two results are bolded and highlighted in **red** and **blue**, respectively.

Dataset		Human (Top-1 Acc. (%))	Model (Top-1 Acc. (%))								
			Baseline	VGG16	ResNet18	ResNet101	ViT-L-16	Swin-B	ConvNeXt -B	MambaOut -B	Ours (ICPNet)
MNIST (Original)		–	99.55	99.41	99.70	99.72	97.23	98.62	99.45	99.37	99.49
I=4	Hor	98.33	**49.02**	17.18	9.80	9.74	9.06	7.95	11.99	14.02	**81.27**
	UL	98.67	19.09	17.22	9.80	9.74	9.80	**95.74**	8.74	11.49	**77.72**
	UR	98.67	16.65	**16.72**	9.80	9.74	8.63	11.50	10.79	12.77	**70.94**
	Ver	97.67	**22.56**	6.22	9.80	9.74	9.48	9.74	10.39	8.24	**67.43**
I=6	Hor	–	**49.70**	14.40	9.80	9.74	8.34	9.74	10.69	9.32	**98.15**
	UL	–	**40.89**	16.97	9.80	9.74	9.81	9.74	19.07	8.81	**98.73**
	UR	–	**34.76**	14.53	9.80	9.74	9.82	9.74	9.71	24.69	**98.81**
	Ver	–	**48.43**	6.50	9.80	9.74	9.78	10.20	9.95	6.89	**98.50**
I=8	Hor	98.67	**20.46**	17.53	9.80	9.74	9.70	9.80	9.35	11.35	**42.46**
	UL	96.00	**24.98**	12.29	9.80	9.74	10.59	17.68	10.52	12.24	**58.22**
	UR	97.67	**23.32**	13.61	9.80	9.74	10.15	9.74	9.29	18.22	**49.48**
	Ver	94.67	**42.13**	8.58	9.80	9.74	9.06	9.77	20.85	11.35	**35.22**
I=10	Hor	–	17.93	**20.31**	9.80	9.74	7.00	9.74	8.93	10.95	**94.33**
	UL	–	**38.11**	15.34	9.80	9.74	9.67	9.74	14.90	11.36	**97.55**
	UR	–	**25.58**	15.20	9.80	9.74	10.05	9.79	11.00	11.48	**98.08**
	Ver	–	**16.47**	8.42	9.80	9.69	9.83	9.82	12.05	16.05	**95.90**
I=12	Hor	–	12.44	**19.33**	11.35	18.72	10.09	9.73	9.45	11.35	**38.28**
	UL	–	22.82	17.96	9.80	9.74	9.75	9.79	**32.53**	11.35	**35.26**
	UR	–	**18.56**	14.86	9.80	9.74	10.51	9.74	10.32	11.36	**37.73**
	Ver	–	9.88	7.55	11.35	**44.59**	15.83	9.82	23.62	11.35	**27.89**
I=14	Hor	–	**22.47**	13.32	9.80	9.73	10.09	9.76	9.65	8.12	**77.45**
	UL	–	**41.10**	17.90	19.27	20.31	9.83	11.26	10.25	11.35	**93.15**
	UR	–	**31.63**	13.22	11.36	15.16	9.61	10.57	8.86	11.35	**96.18**
	Ver	–	10.85	7.94	9.79	9.94	10.10	9.83	9.80	**14.49**	**86.09**

effectively. Furthermore, the class activation maps reveal that ICPNet focuses more on the foreground overall, which aligns with human intuition (see Fig. 7 for more visual explanations of shape constraints). For example, ICPNet correctly classifies the digit "4" by concentrating on its two top areas, whereas Swin exhibits a more dispersive pattern and pays more attention to the background.

Performance comparison on AG-Fashion-MNIST. To further assess the perception of abutting grating illusory contours, we created the more challenging AG-Fashion-MNIST test set. We trained all networks from scratch on the Fashion-MNIST training set [87] and conducted the evaluation on the AG-Fashion-MNIST test set. Table 7 presents the detailed quantitative results. Overall, the results indicate that ICPNet outperforms the state-of-the-art methods by a significant margin across most pixel intervals. Specifically, our method achieves approximately twice the top-1 accuracy of competing approaches at intervals of 4, 6, 8, 10, and 14, and even higher on some subsets. At interval 12, however, ICPNet shows only average performance, which is consistent with the observations from the AG-MNIST test set. Additionally, the performance on the AG-Fashion-MNIST test set is much lower than that on the AG-MNIST test set. We attribute this difference to the inherently higher classification difficulty of the Fashion-MNIST dataset, where objects exhibit more complex shapes and ambiguous category definitions

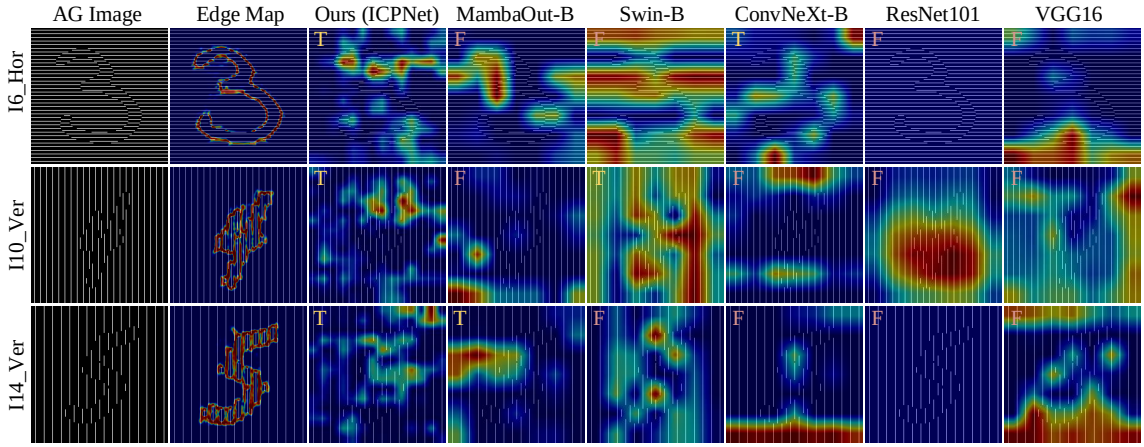

Figure 9. Visual explanations generated by Grad-CAM on the AG-MNIST test set. "Edge Map" refers to the edge prediction map produced by ICPNet. The remaining figures display the Grad-CAM visualizations from the output features of the final convolutional layer for each method. "I", "T", and "F" denote the pixel interval between grating lines, the correct, and incorrect prediction category, respectively. "Hor" and "Ver" represent the illusory contours generated via horizontal and vertical abutting gratings, respectively.

Table 7. Quantitative comparison on Fashion-MNIST and AG-Fashion-MNIST test sets. The first row of results is obtained on the original Fashion-MNIST test set. The best two results are bolded and highlighted in **red** and **blue**, respectively.

Dataset		Model (Top-1 Acc. (%))							
		VGG16	ResNet18	ResNet101	ViT-L-16	Swin-B	ConvNeXt-B	MambaOut-B	Ours(ICPNet)
Fashion-MNIST (Original)		93.99	93.93	93.76	88.32	90.41	93.14	92.40	93.61
I=4	Hor	10.13	10.34	11.04	10.24	12.65	**19.30**	15.97	**44.48**
	UL	10.14	**10.45**	10.14	8.58	9.43	10.08	11.20	**42.69**
	UR	10.14	**10.46**	10.14	10.04	8.22	10.21	12.58	**42.25**
	Ver	10.22	16.21	16.23	8.00	4.34	**21.25**	15.28	**47.81**
I=6	Hor	**15.85**	15.66	13.92	10.23	5.18	10.14	15.93	**68.53**
	UL	10.14	**17.74**	10.04	9.66	12.90	9.53	10.04	**77.15**
	UR	10.14	11.53	**17.92**	10.14	12.63	10.16	16.07	**77.36**
	Ver	14.75	**24.20**	13.31	11.46	10.14	11.27	16.44	**73.83**
I=8	Hor	**21.02**	10.69	10.67	10.08	11.14	12.88	11.40	**48.04**
	UL	10.14	12.49	11.29	9.80	**12.97**	9.37	11.05	**46.39**
	UR	13.29	12.63	11.01	11.77	**17.15**	9.93	11.09	**42.90**
	Ver	**20.64**	18.29	8.65	3.53	3.60	16.67	19.64	**50.42**
I=10	Hor	**26.07**	9.85	14.39	7.69	2.21	14.38	13.44	**52.95**
	UL	10.04	10.66	10.74	6.71	10.14	12.11	**15.53**	**68.51**
	UR	15.59	10.86	6.45	10.89	12.97	10.18	**19.12**	**69.65**
	Ver	**22.80**	9.28	10.86	10.53	17.66	10.92	13.97	**38.75**
I=12	Hor	28.93	**54.74**	27.32	12.98	6.71	10.92	20.82	**34.75**
	UL	11.25	6.71	6.71	12.33	12.54	**20.52**	17.07	**23.95**
	UR	**18.29**	6.75	6.71	10.13	6.22	10.88	17.29	**18.93**
	Ver	**24.55**	**38.25**	9.70	10.74	9.99	12.64	23.33	13.95
I=14	Hor	**27.94**	10.14	10.14	10.14	6.73	10.03	11.59	**36.50**
	UL	14.86	6.77	6.71	10.14	10.08	12.91	**15.06**	**59.34**
	UR	17.29	6.77	6.71	10.06	10.14	10.89	**19.84**	**61.03**
	Ver	**18.30**	7.28	15.49	10.53	10.15	7.03	6.49	**34.05**

compared to the simple digits in the AG-MNIST. Such discrepancies in performance also align with the established

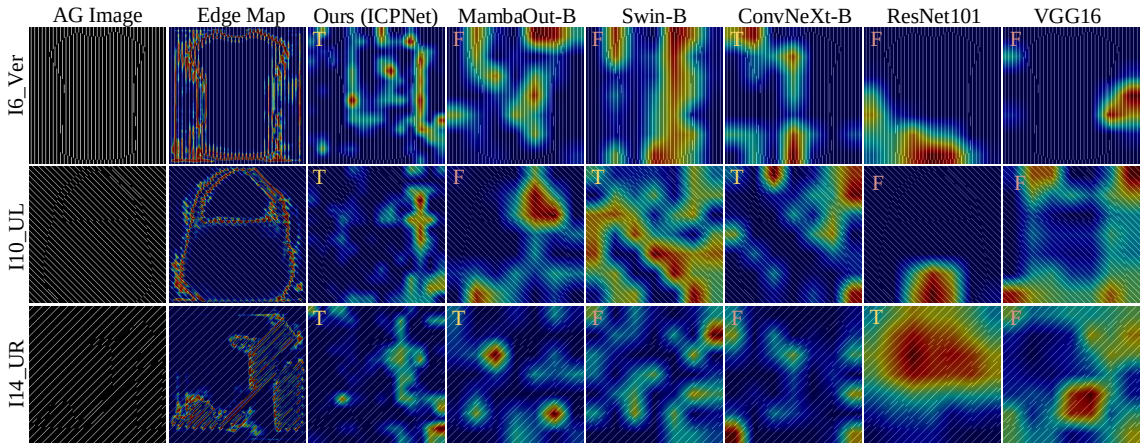

Figure 10. Visual explanations generated by Grad-CAM on the AG-Fashion-MNIST test set. "Edge Map" refers to the edge prediction map produced by ICPNet. The remaining figures display the Grad-CAM visualizations from the output features of the final convolutional layer for each method. "I", "T", and "F" denote the pixel interval between grating lines, the correct, and incorrect prediction category, respectively. "Ver", "UL", and "UR" represent the illusory contour generated via vertical, diagonal from upper left to lower right, and diagonal from upper right to lower left abutting gratings, respectively.

discoveries in human experiments [27]. Critical evaluation reveals that, despite these challenges, ICPNet maintains a higher top-1 accuracy on most abutting grating illusory subsets, indicating a robust ability to perceive illusory contours.

The visual explanations for some models generated by Grad-CAM [93] are shown in Fig. 10. Compared with the edge maps of the AG-MNIST test set, the edge maps of the AG-Fashion-MNIST test set contain more background texture, which may derive from the inherent classification challenge of the dataset. Furthermore, the class activation maps reveal that our model captures multiple key regions for correct predictions. For example, ICPNet correctly classifies the sandal by concentrating on the toe, heel, and other parts, whereas Mambaout pays more attention to the background relatively.

5. Discussion and conclusion

The abutting grating illusory contour is one of the most frequently used illusory figures for investigating shape perception and object recognition in the neuroscience field. Moreover, the abutting grating illusory contour perception represents a sophisticated and fundamental capability in biological visual systems, yet it is notably absent in DNNs, which are employed to simulate biological vision. In this study, inspired by the cortical structures and circuits of the visual systems, we construct a perceptual network with feedback connections, named illusory contour perception network (ICPNet). Extensive experimental results on the AG-MNIST and AG-Fashion-MNIST test sets demonstrate that, although a performance gap remains relative to human performance, ICPNet exhibits obviously conspicuous sensitivity to abutting grating illusory contours compared with other neural networks. This research underscores the critical role played by feedback modulation, attention mechanisms, multi-scale receptive fields, and shape bias in the perception of abutting grating illusory contours. While this study primarily focuses on the abutting grating illusion, we hope that ICPNet with hierarchical feedback connections will inspire the development of more robust networks from the perspective of structural innovation. Moreover, our results emphasize the necessity of fundamental cues (e.g., shape features) for machine perception under extreme distortion conditions. Consequently, the proposed multi-task learning framework holds the potential to inform visual model design in challenging tasks, such as camouflaged object detection [95], occlusion-aware segmentation [96], and underwater object detection [97].

To sum up, illusory contour perception involves multiple cognitive and neural mechanisms. Beyond humans, this ability also serves as an anti-camouflage device in the natural world, enhancing the robustness in object recognition under degraded or occluded conditions for animals [52]. In the era of rapidly evolving AI, the alignment of neural networks with human perception is increasingly crucial, as the ultimate goal of AI is to construct machines that think and perceive like humans [31, 98]. By leveraging visual mechanisms, our model attempts to narrow the gap between the behaviour of DNNs and human visual perception. Our approach presents a promising insight into integrating computer vision with biological vision. Future research will focus on augmenting the ability of model to detect various illusory contours and apply it to natural image understanding tasks.

Acknowledgements This study was supported by the STI2030-Major Projects (2022ZD0204600) and the National

Natural Science Foundation of China (62476050).

References

[1] M. Shishikura, I. Machida, H. Tamura, and K. Sakai, "Local contour features contribute to figure-ground segregation in monkey v4 neural populations and human perception," *Neural Networks*, vol. 181, p. 106821, 2025. 1

[2] F. Schumann, "Einige beobachtungen über die zusammenfassung von gesichtseindrücken zu einheiten," *Zeitschrift Für Psychologie und Physiologie der Sinnesorgane*, vol. 23, pp. 1–32, 1900. 1

[3] G. W. Lesher, "Illusory contours: Toward a neurally based perceptual theory," *Psychonomic Bulletin & Review*, vol. 2, pp. 279–321, 1995. 1, 2

[4] G. Kanizsa, "Subjective contours," *Scientific American*, vol. 234, no. 4, pp. 48–53, 1976. 1, 2, 3

[5] C.-C. Carbon, "Understanding human perception by human-made illusions," *Frontiers in Human Neuroscience*, vol. 8, p. 566, 2014. 1

[6] M. A. Cox, M. C. Schmid, A. J. Peters, R. C. Saunders, D. A. Leopold, and A. Maier, "Receptive field focus of visual area v4 neurons determines responses to illusory surfaces," *Proceedings of the National Academy of Sciences*, vol. 110, no. 42, pp. 17 095–17 100, 2013. 1

[7] J. J. Foxe, E. J. Knight, E. J. Myers, C. Z. Cao, S. Molholm, and E. G. Freedman, "The strength of feedback processing is associated with resistance to visual backward masking during illusory contour processing in adult humans," *Neuroimage*, vol. 259, p. 119416, 2022. 1

[8] D. J. Kalar, P. Garrigan, T. D. Wickens, J. D. Hilger, and P. J. Kellman, "A unified model of illusory and occluded contour interpolation," *Vision research*, vol. 50, no. 3, pp. 284–299, 2010. 1

[9] Y. Pan, M. Chen, J. Yin, X. An, X. Zhang, Y. Lu, H. Gong, W. Li, and W. Wang, "Equivalent representation of real and illusory contours in macaque v4," *Journal of Neuroscience*, vol. 32, no. 20, pp. 6760–6770, 2012. 1, 2, 8

[10] G. E. Smith, P. A. Chouinard, and S.-E. Byosiere, "If i fits i sits: A citizen science investigation into illusory contour susceptibility in domestic cats (felis silvestris catus)," *Applied Animal Behaviour Science*, vol. 240, p. 105338, 2021. 1

[11] A. Pak, E. Ryu, C. Li, and A. A. Chubykin, "Top-down feedback controls the cortical representation of illusory contours in mouse primary visual cortex," *Journal of Neuroscience*, vol. 40, no. 3, pp. 648–660, 2020. 1, 2, 8

[12] P. R. Roelfsema, "Solving the binding problem: Assemblies form when neurons enhance their firing rate—they don't need to oscillate or synchronize," *Neuron*, vol. 111, no. 7, pp. 1003–1019, 2023. 1

[13] M. M. Murray and C. S. Herrmann, "Illusory contours: a window onto the neurophysiology of constructing perception," *Trends in cognitive sciences*, vol. 17, no. 9, pp. 471–481, 2013. 1

[14] G. Sary, K. Köteles, P. Kaposvári, L. Lenti, G. Csifcsák, E. Frankó, G. Benedek, and T. Tompa, "The representation of kanizsa illusory contours in the monkey inferior temporal cortex," *European Journal of Neuroscience*, vol. 28, no. 10, pp. 2137–2146, 2008. 1

[15] T. Fuss, H. Bleckmann, and V. Schluessel, "The brain creates illusions not just for us: sharks (chiloscyllium griseum) can "see the magic" as well," *Frontiers in Neural Circuits*, vol. 8, p. 24, 2014. 1

[16] K. Wyzisk and C. Neumeyer, "Perception of illusory surfaces and contours in goldfish," *Visual neuroscience*, vol. 24, no. 3, pp. 291–298, 2007. 1

[17] A. Nieder and H. Wagner, "Perception and neuronal coding of subjective contours in the owl," *Nature neuroscience*, vol. 2, no. 7, pp. 660–663, 1999. 1

[18] D. M. Eagleman, "Visual illusions and neurobiology," *Nature Reviews Neuroscience*, vol. 2, no. 12, pp. 920–926, 2001. 1

[19] Y. Frégnac and B. Bathellier, "Cortical correlates of low-level perception: from neural circuits to percepts," *Neuron*, vol. 88, no. 1, pp. 110–126, 2015. 1

[20] A. Dosovitskiy, "An image is worth 16x16 words: Transformers for image recognition at scale," *arXiv preprint arXiv:2010.11929*, 2020. 1, 7, 10

[21] K. He, X. Zhang, S. Ren, and J. Sun, "Deep residual learning for image recognition," in *Proceedings of the IEEE conference on computer vision and pattern recognition*, 2016, Conference Proceedings, pp. 770–778. 1, 5, 7, 10

[22] O. Russakovsky, J. Deng, H. Su, J. Krause, S. Satheesh, S. Ma, Z. Huang, A. Karpathy, A. Khosla, and M. Bernstein, "Imagenet large scale visual recognition challenge," *International journal of computer vision*, vol. 115, pp. 211–252, 2015. 1

[23] M. Pu, Y. Huang, Y. Liu, Q. Guan, and H. Ling, "Edter: Edge detection with transformer," in *Proceedings of the IEEE conference on computer vision and pattern recognition*, 2022, Conference Proceedings, pp. 1402–1412. 1

[24] C. Zhou, Y. Huang, M. Pu, Q. Guan, R. Deng, and H. Ling, "Muge: Multiple granularity edge detection," in *Proceedings of the IEEE conference on computer vision and pattern recognition*, 2024, Conference Proceedings, pp. 25 952–25 962. 1

[25] K. Fukushima and S. Miyake, "Neocognitron: A self-organizing neural network model for a mechanism of visual pattern recognition," in *Competition and Cooperation in Neural Nets*, 1982, Conference Proceedings, pp. 267–285. 1

[26] D. H. Hubel and T. N. Wiesel, "Receptive fields, binocular interaction and functional architecture in the cat's visual cortex," *The Journal of Physiology*, vol. 160, no. 1, pp. 106–154, 1962. 1

[27] J. Fan and Y. Zeng, "Challenging deep learning models with image distortion based on the abutting grating illusion," *Patterns*, vol. 4, no. 3, 2023. 1, 2, 3, 6, 7, 10, 11, 13

[28] N. Baker, G. Erlikhman, P. J. Kellman, and H. Lu, "Deep convolutional networks do not perceive illusory contours," in *Proceedings of the annual meeting of the cognitive science society*, vol. 40, 2018, Conference Proceedings. 1, 2

[29] J. S. Bowers, G. Malhotra, M. Dujmović, M. L. Montero, C. Tsvetkov, V. Biscione, G. Puebla, F. Adolfi, J. E. Hummel, and R. F. Heaton, "Deep problems with neural network models of human vision," *Behavioral and Brain Sciences*, vol. 46, p. e385, 2023. 1

[30] Y. Zhang, J. Pan, Y. Zhou, R. Pan, and J. Chai, "Grounding visual illusions in language: Do vision-language models perceive illusions like humans?" in *Conference on Empirical Methods in Natural Language Processing*, 2023, Conference Proceedings, pp. 5718–5728. 1, 3

[31] B. M. Lake, T. D. Ullman, J. B. Tenenbaum, and S. J. Gershman, "Building machines that learn and think like people," *Behavioral and brain sciences*, vol. 40, p. e253, 2017. 2, 13

[32] K. L. Hermann and C. Firestone, "Shape bias at a glance: Comparing human and machine vision on equal terms," *Journal of Vision*, vol. 22, no. 14, pp. 3255–3255, 2022. 2, 4, 5

[33] R. Geirhos, P. Rubisch, C. Michaelis, M. Bethge, F. A. Wichmann, and W. Brendel, "Imagenet-trained cnns are biased towards texture; increasing shape bias improves accuracy and robustness," in *International conference on learning representations*, 2019, Conference Proceedings. 2

[34] S. Grossberg, "How visual illusions illuminate complementary brain processes: illusory depth from brightness and apparent motion of illusory contours," *Frontiers in human neuroscience*, vol. 8, p. 854, 2014. 2, 9

[35] D. H. Grosof, R. M. Shapley, and M. J. Hawken, "Macaque vi neurons can signal 'illusory'contours," *Nature*, vol. 365, no. 6446, pp. 550–552, 1993. 2

[36] E. Peterhans and R. von der Heydt, "Mechanisms of contour perception in monkey visual cortex. ii. contours bridging gaps," *Journal of Neuroscience*, vol. 9, no. 5, pp. 1749–1763, 1989. 2

[37] B. R. Sheth, J. Sharma, S. C. Rao, and M. Sur, "Orientation maps of subjective contours in visual cortex," *Science*, vol. 274, no. 5295, pp. 2110–2115, 1996. 2

[38] R. von der Heydt and E. Peterhans, "Mechanisms of contour perception in monkey visual cortex. i. lines of pattern discontinuity," *Journal of Neuroscience*, vol. 9, no. 5, pp. 1731–1748, 1989. 2, 10

[39] R. von der Heydt, E. Peterhans, and G. Baumgartner, "Illusory contours and cortical neuron responses," *Science*, vol. 224, no. 4654, pp. 1260–1262, 1984. 2

[40] T. S. Lee and M. Nguyen, "Dynamics of subjective contour formation in the early visual cortex," *Proceedings of the National Academy of Sciences*, vol. 98, no. 4, pp. 1907–1911, 2001. 2

[41] G. Kanizsa, "Margini quasi-percettivi in campi con stimolazione omogenea," *Rivista di psicologia*, vol. 49, no. 1, pp. 7–30, 1955. 2

[42] D. L. Ringach and R. Shapley, "Spatial and temporal properties of illusory contours and amodal boundary completion," *Vision Research*, vol. 36, no. 19, pp. 3037–3050, 1996. 2

[43] P. De Weerd, R. Desimone, and L. G. Ungerleider, "Cue-dependent deficits in grating orientation discrimination after v4 lesions in macaques," *Visual neuroscience*, vol. 13, no. 3, pp. 529–538, 1996. 2

[44] K. R. Huxlin, R. C. Saunders, D. Marchionini, H.-A. Pham, and W. H. Merigan, "Perceptual deficits after lesions of inferotemporal cortex in macaques," *Cerebral Cortex*, vol. 10, no. 7, pp. 671–683, 2000. 2

[45] T. S. Lee, "The nature of illusory contour computation," *Neuron*, vol. 33, no. 5, pp. 667–668, 2002. 2

[46] J.-F. Knebel and M. M. Murray, "Towards a resolution of conflicting models of illusory contour processing in humans," *Neuroimage*, vol. 59, no. 3, pp. 2808–2817, 2012. 2

[47] G. Sáry, Z. Chadaide, T. Tompa, K. Köteles, G. Kovács, and G. Benedek, "Illusory shape representation in the monkey inferior temporal cortex," *European Journal of Neuroscience*, vol. 25, no. 8, pp. 2558–2564, 2007. 2

[48] J. D. Mendola, A. M. Dale, B. Fischl, A. K. Liu, and R. B. Tootell, "The representation of illusory and real contours in human cortical visual areas revealed by functional magnetic resonance imaging," *Journal of Neuroscience*, vol. 19, no. 19, pp. 8560–8572, 1999. 2

[49] M. M. Murray, G. R. Wylie, B. A. Higgins, D. C. Javitt, C. E. Schroeder, and J. J. Foxe, "The spatiotemporal dynamics of illusory contour processing: combined high-density electrical mapping, source analysis, and functional magnetic resonance imaging," *Journal of Neuroscience*, vol. 22, no. 12, pp. 5055–5073, 2002. 2

[50] J. Bergmann, L. Petro, C. Abbatecola, M. Li, A. Morgan, and L. Muckli, "Cortical depth profiles in primary visual cortex for illusory and imaginary experiences," *Nature Communications*, vol. 15, no. 1, pp. 1–13, 2024. 2, 3

[51] F. L. Cheng, T. Horikawa, K. Majima, M. Tanaka, M. Abdelhack, S. C. Aoki, J. Hirano, and Y. Kamitani, "Reconstructing visual illusory experiences from human brain activity," *Science Advances*, vol. 9, no. 46, p. eadj3906, 2023. 2, 3

[52] A. Nieder, "Seeing more than meets the eye: processing of illusory contours in animals," *Journal of Comparative Physiology A*, vol. 188, pp. 249–260, 2002. 2, 13

[53] W. Lotter, G. Kreiman, and D. Cox, "A neural network trained for prediction mimics diverse features of biological neurons and perception," *Nature machine intelligence*, vol. 2, no. 4, pp. 210–219, 2020. 2

[54] R. P. Rao and D. H. Ballard, "Predictive coding in the visual cortex: a functional interpretation of some extra-classical receptive-field effects," *Nature neuroscience*, vol. 2, no. 1, pp. 79–87, 1999. 2

[55] W. Lotter, G. Kreiman, and D. Cox, "Deep predictive coding networks for video prediction and unsupervised learning," in *International Conference on Learning Representations*, 2017, Conference Proceedings. 2

[56] Z. Pang, C. B. O'May, B. Choksi, and R. VanRullen, "Predictive coding feedback results in perceived illusory contours in a recurrent neural network," *Neural Networks*, vol. 144, pp. 164–175, 2021. 3

[57] L. Deng, "The mnist database of handwritten digit images for machine learning research," *IEEE signal processing magazine*, vol. 29, no. 6, pp. 141–142, 2012. 3, 6, 10

[58] S. O. Dumoulin, "Layers of neuroscience," *Neuron*, vol. 96, no. 6, pp. 1205–1206, 2017. 3

[59] V. B. Mountcastle, "The columnar organization of the neocortex," *Brain: a journal of neurology*, vol. 120, no. 4, pp. 701–722, 1997. 3

[60] A. A. Galakhova, S. Hunt, R. Wilbers, D. B. Heyer, C. P. de Kock, H. D. Mansvelder, and N. A. Goriounova, "Evolution of cortical neurons supporting human cognition," *Trends in cognitive sciences*, vol. 26, no. 11, pp. 909–922, 2022. 3

[61] D. J. Felleman and D. C. Van Essen, "Distributed hierarchical processing in the primate cerebral cortex," *Cerebral cortex (New York, N.Y. : 1991)*, vol. 1, no. 1, pp. 1–47, 1991. 3

[62] Y. Lu, J. Yin, Z. Chen, H. Gong, Y. Liu, L. Qian, X. Li, R. Liu, I. M. Andolina, and W. Wang, "Revealing detail along the visual hierarchy: neural clustering preserves acuity from v1 to v4," *Neuron*, vol. 98, no. 2, pp. 417–428. e3, 2018. 3

[63] K. Wagstyl, S. Larocque, G. Cucurull, C. Lepage, J. P. Cohen, S. Bludau, N. Palomero-Gallagher, L. B. Lewis, T. Funck, and H. Spitzer, "Bigbrain 3d atlas of cortical layers: Cortical and laminar thickness gradients diverge in sensory and motor cortices," *PLoS biology*, vol. 18, no. 4, p. e3000678, 2020. 3

[64] V. Garcia-Marin, J. G. Kelly, and M. J. Hawken, "Neuronal composition of processing modules in human v1: laminar density for neuronal and non-neuronal populations and a comparison with macaque," *Cerebral Cortex*, vol. 34, no. 2, p. bhad512, 2024. 3

[65] P. Arbelaez, M. Maire, C. Fowlkes, and J. Malik, "Contour detection and hierarchical image segmentation," *IEEE Transactions on Pattern Analysis and Machine Intelligence*, vol. 33, no. 5, pp. 898–916, 2010. 4, 5

[66] R. Mottaghi, X. Chen, X. Liu, N.-G. Cho, S.-W. Lee, S. Fidler, R. Urtasun, and A. Yuille, "The role of context for object detection and semantic segmentation in the wild," in *Proceedings of the IEEE Conference on Computer Vision and Pattern Recognition*, 2014, Conference Proceedings, pp. 891–898. 4, 5

[67] N. T. Markov, M. M. Ercsey-Ravasz, A. Ribeiro Gomes, C. Lamy, L. Magrou, J. Vezoli, P. Misery, A. Falchier, R. Quilodran, and M.-A. Gariel, "A weighted and directed interareal connectivity matrix for macaque cerebral cortex," *Cerebral cortex*, vol. 24, no. 1, pp. 17–36, 2014. 4

[68] N. T. Markov, J. Vezoli, P. Chameau, A. Falchier, R. Quilodran, C. Huissoud, C. Lamy, P. Misery, P. Giroud, and S. Ullman, "Anatomy of hierarchy: feedforward and feedback pathways in macaque visual cortex," *Journal of Comparative Neurology*, vol. 522, no. 1, pp. 225–259, 2014. 4

[69] T. D. Albright, T. M. Jessell, E. R. Kandel, and M. I. Posner, "Neural science: a century of progress and the mysteries that remain," *Cell*, vol. 100, pp. 1–55, 2000. 4

[70] S. Shushruth, J. M. Ichida, J. B. Levitt, and A. Angelucci, "Comparison of spatial summation properties of neurons in macaque v1 and v2," *Journal of neurophysiology*, vol. 102, no. 4, pp. 2069–2083, 2009. 4

[71] B. A. Wandell and J. Winawer, "Computational neuroimaging and population receptive fields," *Trends in cognitive sciences*, vol. 19, no. 6, pp. 349–357, 2015. 5

[72] F. Y. Yu and V. Koltun, "Multi-scale context aggregation by dilated convolutions," in *International Conference on Learning Representations*, 2015, Conference Proceedings, pp. 1–13. 5

[73] A. G. Howard, M. Zhu, B. Chen, D. Kalenichenko, W. Wang, T. Weyand, M. Andreetto, and H. Adam, "Mobilenets: Efficient convolutional neural networks for mobile vision applications," *arXiv preprint arXiv:1704.04861*, 2017. 5

[74] Z. Liu, Y. Lin, Y. Cao, H. Hu, Y. Wei, Z. Zhang, S. Lin, and B. Guo, "Swin transformer: Hierarchical vision transformer using shifted windows," in *IEEE International Conference on Computer Vision*, 2021, Conference Proceedings, pp. 10 012–10 022. 5, 7, 10

[75] J. L. Ba, J. R. Kiros, and G. E. Hinton, "Layer normalization," *arXiv preprint arXiv:1607.06450*, 2016. 5

[76] M. Levinson, E. Podvalny, S. Baete, and B. He, "Cortical and subcortical signatures of conscious object recognition," *Nature Communications*, vol. 12, no. 1, pp. 1–16, 2021. 5

[77] M. Suzuki, C. M. Pennartz, and J. Aru, "How deep is the brain? the shallow brain hypothesis," *Nature Reviews Neuroscience*, vol. 24, no. 12, pp. 778–791, 2023. 5

[78] W. Wang, T. Zhou, L. Chen, and Y. Huang, "A subcortical magnocellular pathway is responsible for the fast processing of topological properties of objects: A transcranial magnetic stimulation study," *Human Brain Mapping*, vol. 44, no. 4, pp. 1617–1628, 2023. 5

[79] Z. Liu, H. Mao, C.-Y. Wu, C. Feichtenhofer, T. Darrell, and S. Xie, "A convnet for the 2020s," in *Proceedings of the IEEE conference on computer vision and pattern recognition*, 2022, Conference Proceedings, pp. 11 976–11 986. 5, 7, 10

[80] C. Xia, X. Wang, F. Lv, X. Hao, and Y. Shi, "Vit-comer: Vision transformer with convolutional multi-scale feature interaction for dense predictions," in *Proceedings of the IEEE conference on computer vision and pattern recognition*, 2024, Conference Proceedings, pp. 5493–5502. 5

[81] X. Zhang, X. Zhou, M. Lin, and J. Sun, "Shufflenet: An extremely efficient convolutional neural network for mobile devices," in *Proceedings of the IEEE conference on computer vision and pattern recognition*, 2018, Conference Proceedings, pp. 6848–6856. 5

[82] S. Woo, J. Park, J.-Y. Lee, and I. S. Kweon, "Cbam: Convolutional block attention module," in *European Conference on Computer Vision*, ser. Computer Vision – ECCV 2018, 2018, Conference Proceedings, pp. 3–19. 5

[83] X. Dong, J. Bao, D. Chen, W. Zhang, N. Yu, L. Yuan, D. Chen, and B. Guo, "Cswin transformer: A general vision transformer backbone with cross-shaped windows," in *Proceedings of the IEEE conference on computer vision and pattern recognition*, 2022, Conference Proceedings, pp. 12 124–12 134. 5

[84] X. Zhang, C. Lin, F. Li, Y. Cao, and Y. Li, "Lvp-net: A deep network of learning visual pathway for edge detection," *Image and Vision Computing*, vol. 147, p. 105078, 2024. 5, 6, 7

[85] D. Hendrycks and K. Gimpel, "Gaussian error linear units (gelus)," *arXiv preprint arXiv:1606.08415*, 2016. 5

[86] S. Xie and Z. Tu, "Holistically-nested edge detection," in *International Conference on Computer Vision*, 2015, Conference Proceedings, pp. 1395–1403. 6, 7

[87] H. Xiao, K. Rasul, and R. Vollgraf, "Fashion-mnist: a novel image dataset for benchmarking machine learning algorithms," *arXiv preprint arXiv:1708.07747*, 2017. 6, 11

[88] A. Kirillov, E. Mintun, N. Ravi, H. Mao, C. Rolland, L. Gustafson, T. Xiao, S. Whitehead, A. C. Berg, and W.-Y. Lo, "Segment anything," in *Proceedings of the IEEE international conference on computer vision*, 2023, Conference Proceedings, pp. 4015–4026. 7

[89] N. Otsu, "A threshold selection method from gray-level histograms," *IEEE Transactions on Systems, Man, and Cybernetics*, vol. 9, no. 1, pp. 62–66, 1979. 7

[90] K. Simonyan and A. Zisserman, "Very deep convolutional networks for large-scale image recognition," in *International Conference on Learning Representations*, 2015, Conference Proceedings, pp. 1–14. 7, 10

[91] W. Yu and X. Wang, "Mambaout: Do we really need mamba for vision?" in *Proceedings of the IEEE conference on computer vision and pattern recognition*, 2025, Conference Proceedings. 7, 10

[92] I. Loshchilov and F. Hutter, "Decoupled weight decay regularization," *arXiv preprint arXiv:1711.05101*, 2017. 7

[93] R. R. Selvaraju, M. Cogswell, A. Das, R. Vedantam, D. Parikh, and D. Batra, "Grad-cam: Visual explanations from deep networks via gradient-based localization," in *Proceedings of the IEEE international conference on computer vision*, 2017, Conference Proceedings, pp. 618–626. 9, 10, 13

[94] M. Soriano, L. Spillmann, and M. Bach, "The abutting grating illusion," *Vision research*, vol. 36, no. 1, pp. 109–116, 1996. 9, 10

[95] H. Bi, C. Zhang, K. Wang, J. Tong, and F. Zheng, "Rethinking camouflaged object detection: Models and datasets," *IEEE transactions on circuits and systems for video technology*, vol. 32, no. 9, pp. 5708–5724, 2021. 13

[96] L. Ke, Y.-W. Tai, and C.-K. Tang, "Occlusion-aware instance segmentation via bilayer network architectures," *IEEE Transactions on Pattern Analysis and Machine Intelligence*, vol. 45, no. 8, pp. 10 197–10 211, 2023. 13

[97] A. Jesus, C. Zito, C. Tortorici, E. Roura, and G. De Masi, "Underwater object classification and detection: first results and open challenges," *OCEANS 2022-chennai*, pp. 1–6, 2022. 13

[98] L. M. Schulze Buschoff, E. Akata, M. Bethge, and E. Schulz, "Visual cognition in multimodal large language models," *Nature Machine Intelligence*, vol. 7, no. 1, pp. 96–106, 2025. 13